Journal of Computational Science 10 (2015) 45–54

Contents lists available at ScienceDirect

Journal of Computational Science

journal homepage: www.elsevier.com/locate/jocs

Aerodynamic shape optimization by variable-fidelity computational fluid dynamics models: A review of recent progress

Leifur Leifsson [a,*], Slawomir Koziel [b]

[a] Iowa State University, Ames, IA 50011, USA
[b] Faculty of Electronics, Telecommunications and Informatics, Gdansk University of Technology, 80-233 Gdansk, Poland

ARTICLE INFO

Article history:
Received 23 November 2013
Received in revised form 2 September 2014
Accepted 22 January 2015
Available online 11 February 2015

Keywords:
Surrogate-based optimization
Variable-fidelity modeling
Aerodynamics
Computational fluid dynamics
Airfoil shape design

ABSTRACT

A brief review of some recent variable-fidelity aerodynamic shape optimization methods is presented. We discuss three techniques that—by exploiting information embedded in low-fidelity computational fluid dynamics (CFD) models—are able to yield a satisfactory design at a low computational cost, usually corresponding to a few evaluations of the original, high-fidelity CFD model to be optimized. The specific techniques considered here include multi-level design optimization, space mapping, and shape-preserving response prediction. All of them use the same prediction–correction scheme, however, they differ in the way the low-fidelity model information it utilized to construct the surrogate model. The presented techniques are illustrated using three specific cases of transonic airfoil design involving lift maximization and drag minimization.

1. Introduction

Aerodynamic (or hydrodynamic) shapes and surfaces are encountered in numerous engineering systems, such as aircraft, automobiles, ships, rockets, bicycles, turbines, and pumps; just to name a few. The task of the aerodynamic engineer is to find a shape (or adjust the existing one) that improves a given aerodynamic measure of merit while adhering to appropriate constraints. The complexity of engineering systems is growing and computer simulations are needed to provide a reliable evaluation of system performance. Given the nonlinear behavior of fluid systems it is often an impossible task to improve a given design by using a hands-on approach. Numerical design techniques are, therefore, essential to assist the engineer in solving the challenging task. Aerodynamic shape optimization (ASO) involves the use of search algorithms for the design of aerodynamic surfaces. This paper provides a review of recent progress in this field. In particular, several variable-fidelity optimization algorithms, which have been shown to be very efficient, will be described and compared with benchmark techniques.

Hicks et al. [1] are generally credited for the first practical application of ASO. They used a conjugate-gradient method to design two-dimensional airfoil shapes in transonic flow. Later, Hicks and Henne [2] extend the work to three-dimensional transonic wing design with a steepest-descent gradient method. Nowadays, gradient-based methods are considered the state-of-the-art in ASO and are the most widely used approaches; see for example [3–6]. The key to using gradient-based ASO is the adjoint approach, first introduced by Pironneau [7], and later developed for aerodynamic design by Jameson [8]. The main advantage is that the cost of a gradient calculation can be made nearly independent of the number of design variables. This opens the gateway for applying ASO to problems with a large design space.

Various other types of algorithms are used for ASO, such as derivative-free methods, one-shot methods, and surrogate-based methods. Evolutionary algorithms, such as genetic algorithms, are the most popular derivative-free methods for ASO; see for example Holst and Pulliam [9], and Epstein and Peigin [10]. The fundamental advantage of evolutionary algorithms (or, more broadly, population-based metaheuristics) over gradient-based ones is their ability to perform global search. However, this comes at a price since a large number of model evaluations are needed, especially for a large design space. One-shot methods are based on the same Lagrangian formulation as the gradient-based methods, but the flow equations and the first-order optimality conditions are solved simultaneously, and, thereby, avoiding repeated flow and gradient evaluations. An overview of the approach can be found in Gunzburger [11] and applications can be found in Gatsis and Zingg [12], and Iollo et al. [13].

In surrogate-based optimization (SBO), a computationally expensive model is replaced by a cheap surrogate model [14,15].

* Corresponding author. Tel.: +1 515 294 6549.
E-mail address: leifur@iastate.edu (L. Leifsson).

http://dx.doi.org/10.1016/j.jocs.2015.01.003
1877-7503/

The main objective is to accelerate the optimization process and obtain an optimized design by using fewer evaluations of the expensive model. Typically, the surrogates are functional ones, i.e., constructed by using design of experiments and data fitting. A variety of techniques are available to create function-approximation surrogate models. These include polynomial regression [14], radial basis function interpolation [15], kriging [16], and support vector regression [17]. Function-approximation models are versatile, however, they normally require substantial amount of data samples to ensure good accuracy. Examples of SBO with various function–approximation models related to aerodynamic design can be found in Forrester et al. [18], Jouhoud et al. [19], and Brooks et al. [20].

Variable-fidelity optimization (VFO) refers to a certain type of SBO where the surrogate models are constructed using corrected physics-based low-fidelity models [21–29]. The low-fidelity models can be obtained using one of, or a combination of the following: simplified physics models (also called variable-fidelity physics models), the high-fidelity model with a coarser computational mesh discretization (called variable-resolution models), and relaxed flow solver convergence criteria (called variable-accuracy models). The surrogate model needs to be a reliable representation of the high-fidelity model. This is typically achieved by correcting the low-fidelity model. Examples of correction techniques for aerodynamic models include space mapping (SM) [24,27], shape-preserving response prediction (SPRP) [25,28], and adaptive response correction (ARC) [29]. The key benefit of the VFO approach is that compared to function-approximation surrogates, less high-fidelity model data may be needed to construct a physics-based one to obtain a given accuracy level, which will lead to improved algorithm efficiency.

In this paper, we provide a brief summary of recently developed VFO algorithms for the design of aerodynamic surfaces. In particular, we describe the multi-level optimization (MLO) algorithm [23], and the SM [24] and SPRP [28] correction techniques. The algorithms are applied to aerodynamic shape optimization of transonic airfoils.

2. Aerodynamic shape optimization

This section provides a discussion on the basic properties and characteristics of aerodynamic surfaces pertaining to the geometry and the performance measures, as well as an example of design objectives. A mathematical formulation of the ASO problem is given.

2.1. Basic characteristics of aerodynamic surfaces

Aerodynamic shapes are typically described by a set of parameters and shape functions. For example, the aircraft wing shown in Fig. 1 can be described on one hand by planform variables, such as the span (b), sweep (Λ), and chord lengths (c) shown in Fig. 1(a), and, on the other hand by the airfoil shapes at each spanstation, such as the root, kink, and tip. Each airfoil section, such as the one in Fig. 1(b), can be described by a set of shape functions and parameters.

2.2. Aerodynamic performance metrics

The measure of merit is a quantity that characterizes the performance of the aerodynamic surface. The characteristics of an aerodynamic surface are typically represented with the non-dimensional coefficients of forces, pressures, and moments acting on it, such as the coefficients of lift (C_l), drag (C_d), pressure (C_p), and pitching moment (C_M).

The performance metrics are, typically, obtained by aerodynamic analysis of the streamlined surfaces through computational fluid dynamics (CFD) simulations. CFD models contain, in general, the following elements: geometry modeling and parameterization, computational grid generation, flow solution, and a calculation of the measures of merit. The entire process is automated and integrated within an optimization framework. The simulation of the flow about a typical transport wing could take around 24 h (assuming a parallel computation on 8 processors). Obviously, a more powerful hardware will reduce the computational time. A computation of the two-dimensional flow past an airfoil needs around 0.5 million grid cells and takes around half an hour (on a similar machine).

Typically, the objective is to minimize the drag. For example, in the design of transonic wings one of the main objectives is to minimize the drag induced by a pressure shock, such as the one shown in Fig. 2. Often, in low speed design the objective is to maximize the lift. Maximization of the lift to drag ratio can also be considered. Anderson [30] provides an excellent discussion of aerodynamic design of transonic airfoils and wings.

2.3. Constraints

There can be constraints pertaining to various aspects of the engineering system under consideration. Aircraft design is highly multi-disciplinary and the constraints can be related to the aerodynamics, structures, propulsion system, and control systems. As all the disciplines are highly coupled, ASO needs to account for that in some way. For example, the wings of an aircraft have many structural, mechanical, and electrical components. There needs to be space for these components. This is often accounted for in ASO by thickness constraints.

2.4. Problem formulation

ASO can be formulated as a constrained nonlinear minimization problem, i.e., for a given operating condition, solve

$$x^* = \underset{x}{\operatorname{argmin}} H(f(x)), \text{ s.t.} g_j(x) \leq 0, h_k(x) = 0, l \leq x \leq u, \quad (1)$$

where H is the objective function, $f(x)$ is the high-fidelity model, x^* is the optimized design, x is the design variable vector (describing the airfoil shape), arg min represents minimization, $g_j(x)$ are the inequality constraints with $j = 1,\ldots, M$, $h_k(x)$ are the equality constraints with $k = 1,\ldots, N$, and l and u are the lower and upper bounds of the design variables, respectively.

The detailed formulation then depends on the particular design scenario. Typically, lift maximization and drag minimization can

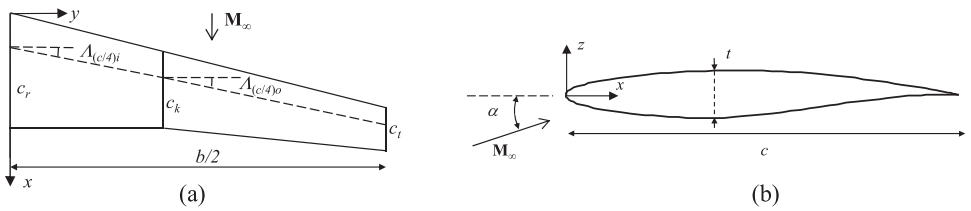

Fig. 1. Nomenclature for typical transonic aircraft wing geometry, (a) planform view, (b) airfoil section.

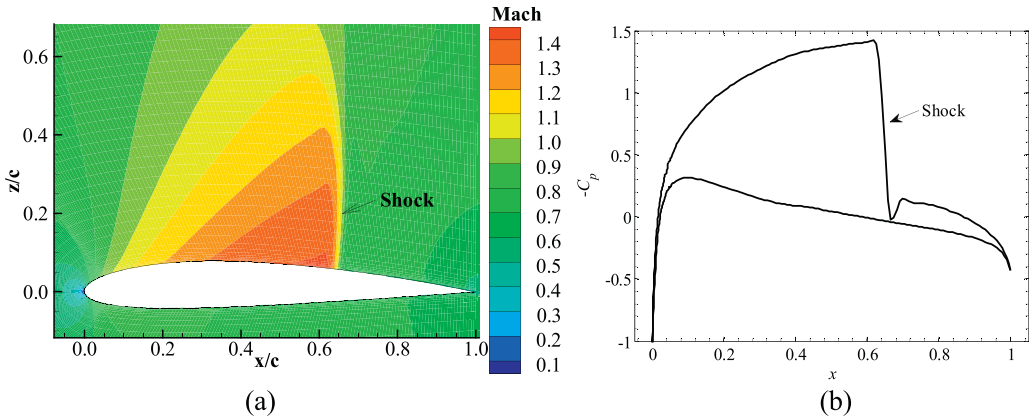

Fig. 2. Inviscid transonic flow analysis of NACA 2412 at Mach 0.75 and an angle of attack of 1° with the compressible Euler equations: (a) contours of Mach number and (b) surface pressure distribution. The lift coefficient is $C_l = 0.67$ and drag coefficient $C_d = 0.0261$.

be considered with the following formulation (drag minimization is given in parenthesis): for a given operating condition (such as the Mach number M_∞ (defined as the ratio of freestream flow velocity to the speed of sound) and an angle of attack α (see definition in Fig. 1(b))), minimize the negative section lift coefficient, $f(x) = -C_l(x)$ (minimize the section drag coefficient, $f(x) = C_d(x)$), subject to constraints on the section drag coefficient, $g_1(x) = C_d(x) - C_{d.\max} \leq 0$ ($g_1(x) = C_{l.\min} - C_l(x) \leq 0$), and the cross-sectional area of the airfoil section (A), $g_2(x) = A_{\min} - A(x) \leq 0$.

3. Variable-fidelity solution approaches

In this section, we first discuss the SBO concept, which is the basis of VFO, and then we describe the three different VFO algorithms.

3.1. SBO Concept

In general, the SBO approach does not attempt to solve the original problem (1) directly. Instead, a sequence of approximate solutions are generated, $x^{(i)}$, $i = 0, 1, \ldots$, ($x^{(0)}$ is the initial design) as

$$x^{(i+1)} = \underset{x}{\operatorname{argmin}} H\left(s^{(i)}(x)\right), \tag{2}$$

where $s^{(i)}(x)$ is the surrogate model at iteration i. The flow of a generic SBO algorithm is shown in Fig. 3.

The surrogate models can be constructed by approximating sampled high-fidelity model data using regression (so-called function-approximation surrogates) (see, e.g., [1,2]), or by correcting physics-based low-fidelity models which are less accurate but a computationally cheaper representations of the high-fidelity models (see, e.g., [3,4]). In algorithm (2), the high-fidelity model f is usually referenced rarely (sometimes even once per iteration, at every new design $x^{(i+1)}$) for verification purposes and to obtain the data necessary to update the surrogate model. Normally, the surrogate model is much cheaper (in computational terms) than f so that its optimization cost does not contribute significantly to the overall optimization cost (which, in turn, is mostly determined by the number of high-fidelity model evaluations). The key point is that the number of evaluations of f for a well performing SBO algorithm is substantially smaller than for any direct optimization method (e.g., gradient-based one) [31]. If the surrogate model satisfies zero- and first-order consistency conditions with the high-fidelity model, i.e., $s^{(i)}(x^{(i)}) = f(x^{(i)})$ and $(\partial s^{(i)}/\partial x)(x^{(i)}) = (\partial f/\partial x)(x^{(i)})$ (verification of the latter requires f sensitivity data), and the algorithm (2) is enhanced by the trust region method [31,32], then it is provably convergent to a local optimum of the high-fidelity model [33]. Convergence can also be guaranteed if the algorithm (2) is enhanced by properly selected local search methods [34]. For many practical SBO algorithms, especially with physics-based surrogates, only the zero-order consistency is preserved, however, this is usually sufficient in combination with the knowledge about the system embedded in the low-fidelity model.

Three SBO algorithms using physics-based surrogate models are described in this paper. The main commonality of the algorithms is that they employ variable-resolution computational fluid dynamics (CFD) models. They differ mainly in the way how the surrogate models are corrected.

3.2. Multi-level optimization

The MLO algorithm [5] exploits a family of low-fidelity models, denoted as $\{c_j\}$, $j = 1, \ldots, K$, all evaluated by the same CFD solver as the one used for the high-fidelity model f. Discretization of the model c_{j+1} is finer than that of the model c_j, which results in a better accuracy but also a longer evaluation time. In practice, $K = 2$ or 3. The discretization density may be controlled by solver-dependent parameters (e.g., the meshing parameters).

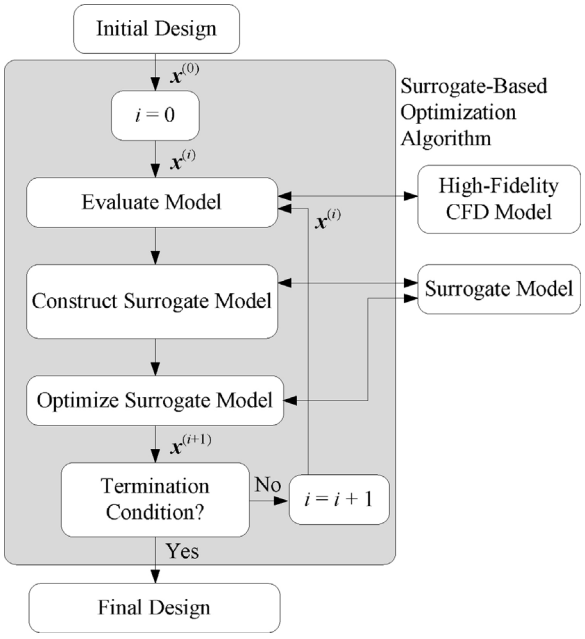

Fig. 3. The flow of a generic surrogate-based optimization (SBO) algorithm.

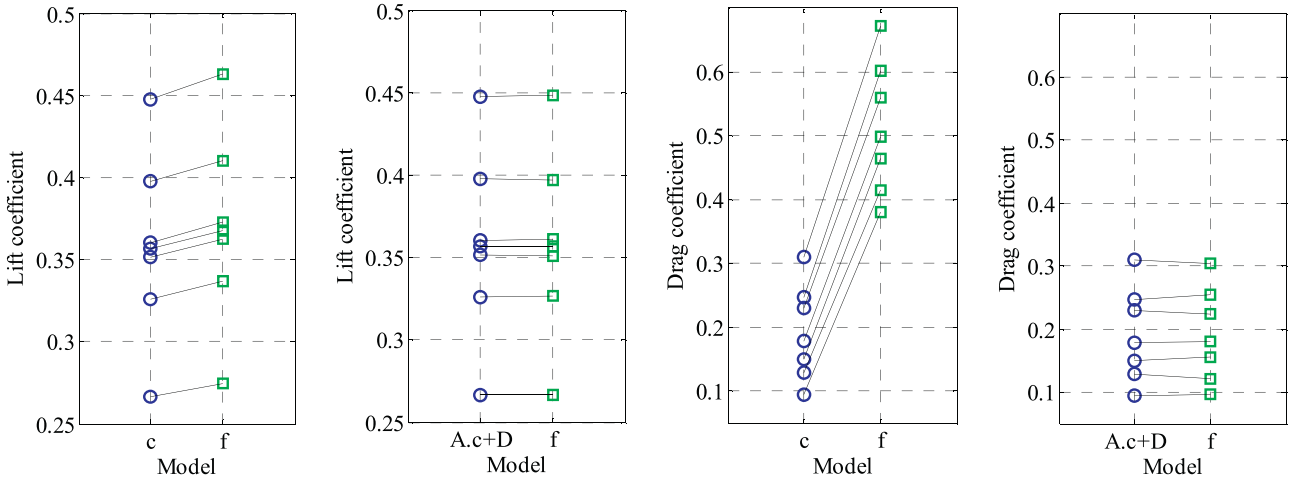

Fig. 4. The effect of output SM (8) on the low- and high-fidelity CFD model (described in Section 4) alignment.

The optimization procedure works as follows. Starting from the initial design $x^{(0)}$, the coarsest model c_1 is optimized to produce a first approximation of the high-fidelity model optimum, $x^{(1)}$. The vector $x^{(1)}$ is used as a starting point to find the next approximation of the high-fidelity model optimum, $x^{(2)}$, which is obtained by optimizing the next model, c_2. The process continues until the optimum $x^{(K)}$ of the last low-fidelity model c_K.

Having $x^{(K)}$, we evaluate the model c_K at all perturbed designs around $x^{(K)}$, i.e., at $x_k{}^{(K)} = [x_1{}^{(K)} \ldots x_k{}^{(K)} + \text{sign}(k)\cdot d_k \ldots x_n{}^{(K)}]^T$, $k = -n, -n+1, \ldots, n-1, n$. We use the notation $c^{(k)} = c_K(x_k{}^{(K)})$. This data is used to refine the final design without directly optimizing the high-fidelity model f. More specifically, we set up an approximation model involving $c^{(k)}$ and optimize it in the neighborhood of $x^{(K)}$ defined as $[x^{(K)} - d, x^{(K)} + d]$, where $d = [d_1\ d_2 \ldots d_n]^T$. The size of the neighborhood can be selected based on a sensitivity analysis of c_1 (the cheapest of the low-fidelity models); usually d equals 2 to 5 percent of $x^{(K)}$.

Here, an approximation is performed using a reduced quadratic model $q(x) = [q_1\ q_2 \ldots q_m]^T$, defined as

$$q_j(x) = q_j([x_1 \ldots x_n]^T) = \lambda_{j.0} + \lambda_{j.1}x_1 + \ldots + \lambda_{j.n}x_n + \lambda_{j.n+1}x_1^2 + \ldots + \lambda_{j.2n}x_n^2 \quad (3)$$

The coefficients $\lambda_{j.r}, j = 1, \ldots, m, r = 0, 1, \ldots, 2n$, are uniquely obtained by solving a linear regression problem

$$\begin{bmatrix} 1 & x_{-n.1}^{(K)} & \cdots & x_{-n.n}^{(K)} & \left(x_{-n.1}^{(K)}\right)^2 & \cdots & \left(x_{-n.n}^{(K)}\right)^2 \\ \vdots & \vdots & & \vdots & \vdots & & \vdots \\ 1 & x_{0.1}^{(K)} & \cdots & x_{0.n}^{(K)} & \left(x_{0.1}^{(K)}\right)^2 & \cdots & \left(x_{-n.n}^{(K)}\right)^2 \\ \vdots & \vdots & & \vdots & \vdots & & \vdots \\ 1 & x_{n.1}^{(K)} & \cdots & x_{n.n}^{(K)} & \left(x_{n.1}^{(K)}\right)^2 & \cdots & \left(x_{-n.n}^{(K)}\right)^2 \end{bmatrix} \times \begin{bmatrix} \lambda_{j.0} \\ \lambda_{j.1} \\ \vdots \\ \lambda_{j.2n} \end{bmatrix} = \begin{bmatrix} c_j^{(-n)} \\ \vdots \\ c_j^{(0)} \\ \vdots \\ c_j^{(n)} \end{bmatrix} \quad (4)$$

where $x_{k.j}{}^{(K)}$ is a jth component of the vector $x_k{}^{(K)}$, and $c_j{}^{(k)}$ is a jth component of the vector $c^{(k)}$.

In order to account for the unavoidable misalignment between c_K and f, instead of optimizing the quadratic model q, it is recommended to optimize a corrected model $q(x) + [f(x^{(K)}) - c_K(x^{(K)})]$, thus, ensuring a zero-order consistency between c_K and f. The refined design can be then found as

$$x^* = \arg \min_{x^{(K)}-d \le x \le x^{(K)}+d} H\left(q(x) + \left[f\left(x^{(K)}\right) - c_K\left(x^{(K)}\right)\right]\right) \quad (5)$$

This kind of correction is also known as output SM [9]. If necessary, step (5) can be performed a few times starting from a refined design, i.e., $x^* = \arg \min\{x^{(K)} - d \le x \le x^{(K)} + d: H(q(x) + [f(x^*) - c_K(x^*)])\}$. It should be noted that the high-fidelity model is not evaluated until executing the refinement step (5). Also, each refinement iteration requires only a single evaluation of f.

The optimization procedure can be summarized as follows (where K is the number of models):

1. set $j = 1$;
2. select the initial design $x^{(0)}$;
3. starting from $x^{(j-1)}$ find $x^{(j)} = \arg \min\{x: H(c_j(x))\}$;
4. set $j = j + 1$; if $j < K$ go to 3;
5. obtain a refined design according to (5).

3.3. Space mapping

SM [6] works directly on the figures of interest. The surrogate model is a composition of the low-fidelity model and simple, usually linear, transformations [9]. A generic SM surrogate model can be written as $s(x,p)$, where p represents model parameters. The surrogate at iteration i is then

$$s^{(i)}(x) = s\left(x, p^{(i)}\right), \quad (6)$$

with the parameters $p^{(i)}$ determined through so-called parameter extraction (PE) process [9] to minimize misalignment between the surrogate and the high-fidelity model at some or all previous iterations points, where the high-fidelity data is already available. Parameter extraction is, in general, solved as a nonlinear minimization problem of the form

$$p^{(i)} = \arg\min_p \sum_{k=0}^{i} \left\| f\left(x^{(k)}\right) - s\left(x^{(k)}, p\right) \right\|^2 \quad (7)$$

where $|\times|^2$ is the L^2 norm.

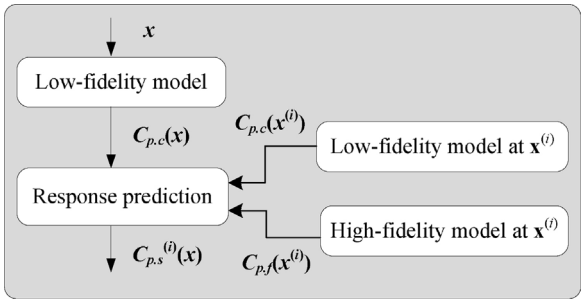

Fig. 5. Surrogate model construction at design iteration i using the shape-preserving response prediction technique.

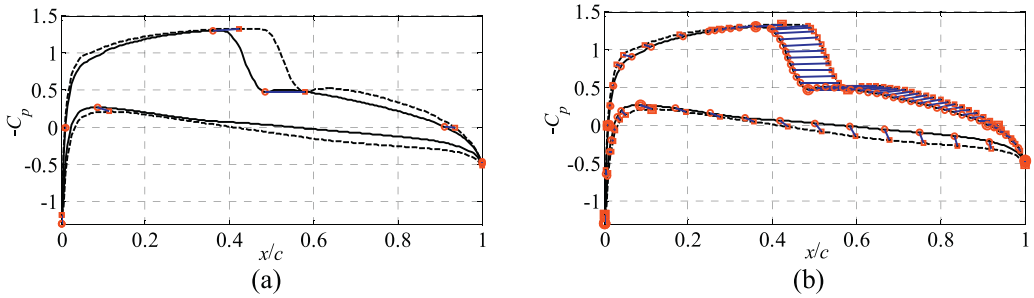

Fig. 6. An illustration of the SPRP technique applied to the pressure distributions obtained by the low-fidelity CFD models of two designs: (a) initial characteristic points and translation vectors, (b) additional points.

In aerodynamic shape optimization, typically the lift and drag coefficients are the figures of merit. Let's assume that the high-fidelity model is defined as $f(x) = [C_{l.f}(x)\, C_{d.f}(x)\, A_f(x)]^T$, where $C_{l.f}$ and $C_{d.f}$ are (high-fidelity CFD-simulated) section lift and drag coefficients, whereas A_f is an airfoil cross-sectional area. The space mapping surrogate model at iteration i can then be defined as $s^{(i)}(x) = [C_{l.s}{}^{(i)}(x)\, C_{d.s}{}^{(i)}(x)\, A_s{}^{(i)}(x)]^T$.

One of the problems with applying space mapping to aerodynamic design is that the low-fidelity CFD model is relatively expensive, which may result in a substantial computational overhead related to the parameter extraction (7). This problem can be overcome by using output SM surrogate models since their parameters can be calculated analytically. More specifically, the surrogate model is based on both multiplicative and additive response corrections of the form

$$s^{(i)}(x) = A^{(i)} \circ c(x) + D^{(i)} + q^{(i)} = [a_l^{(i)} C_{l.c}(x) + d_l^{(i)} + q_l^{(i)} a_d^{(i)} C_{d.c}(x) + d_d^{(i)} + q_d^{(i)} A_c(x)]^T, \quad (8)$$

where $\circ$ denotes a component-wise multiplication. Note that there is no need to map A_c because $A_c(x) = A_f(x)$ for all x. The response correction parameters $A^{(i)}$ and $D^{(i)}$ are obtained as

$$[A^{(i)}, D^{(i)}] = \arg\min_{[A,D]} \sum_{k=0}^{i} \| f(x^{(k)}) - A \circ c(x^{(k)}) + D \|^2, \quad (9)$$

i.e., the response scaling is supposed to (globally) improve the matching for all previous iteration points. The additive response correction term $q^{(i)}$ is defined as

$$q^{(i)} = f\left(x^{(i)}\right) - \left[A^{(i)} \circ c\left(x^{(i)}\right) + D^{(i)}\right], \quad (10)$$

i.e., it ensures a perfect match of the surrogate and the high-fidelity model at the current design $x^{(i)}$, $s^{(i)}(x^{(i)}) = f(\boldsymbol{x}^{(i)})$ (so-called zero-order consistency).

Both $A^{(i)}$, $D^{(i)}$ and $q^{(i)}$ can be calculated analytically so that there is no need to carry out a nonlinear-minimization-like PE process (7). The term $q^{(i)}$ can be calculated using (10). Terms $A^{(i)}$ and $D^{(i)}$ can be obtained as

$$\begin{bmatrix} a_l^{(i)} \\ d_l^{(i)} \end{bmatrix} = \left(C_l^T C_l\right)^{-1} C_l^T F_l, \quad \begin{bmatrix} a_l^{(i)} \\ d_l^{(i)} \end{bmatrix} = \left(C_d^T C_d\right)^{-1} C_d^T F_d \quad (11)$$

where

$$C_l = \begin{bmatrix} C_{l.c}\left(x^{(0)}\right) & C_{l.c}\left(x^{(1)}\right) & \cdots & C_{l.c}\left(x^{(i)}\right) \\ 1 & 1 & \cdots & 1 \end{bmatrix}^T,$$

$$F_l = \begin{bmatrix} C_{l.f}\left(x^{(0)}\right) & C_{l.f}\left(x^{(1)}\right) & \cdots & C_{l.f}\left(x^{(i)}\right) \\ 1 & 1 & \cdots & 1 \end{bmatrix}^T$$

$$C_d = \begin{bmatrix} C_{d.c}\left(x^{(0)}\right) & C_{d.c}\left(x^{(1)}\right) & \cdots & C_{d.c}\left(x^{(i)}\right) \\ 1 & 1 & \cdots & 1 \end{bmatrix}^T,$$

$$C_d = \begin{bmatrix} C_{d.f}\left(x^{(0)}\right) & C_{d.f}\left(x^{(1)}\right) & \cdots & C_{d.f}\left(x^{(i)}\right) \\ 1 & 1 & \cdots & 1 \end{bmatrix}^T$$

which is a least-square optimal solution to the linear regression problem $C_l a_l^{(i)} + d_l^{(i)} = F_l$, and $C_d a_d^{(i)} + d_d^{(i)} = F_d$, equivalent to (9). Note that the matrices $C_l{}^T C_l$ and $C_d{}^T C_d$ are non-singular for $i > 1$. For $i = 1$, only the multiplicative correction with $A^{(i)}$ components are used, which can be calculated in a similar way. Fig. 4 shows an example of the application of output SM to an airfoil CFD model.

3.4. Shape-preserving response prediction

The lift and drag coefficients can be obtained by integrating the pressure coefficient (C_p) (and the skin friction coefficient (C_f) in a viscous analysis) over the surface of the airfoil or wing. The SPRP technique [7,8] works on the level of the pressure distribution. By

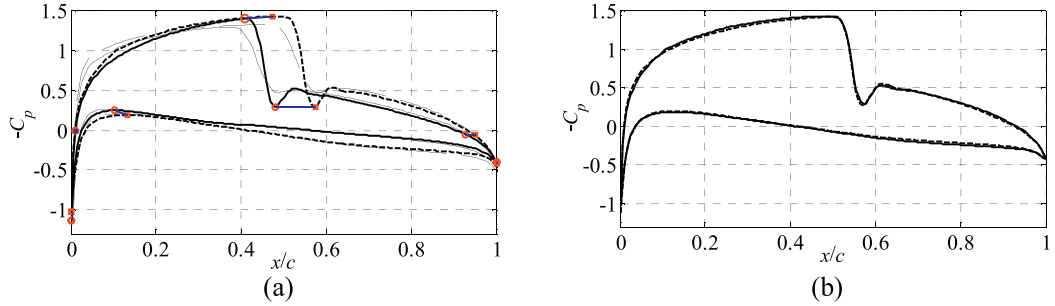

Fig. 7. Application of SPRP to the high-fidelity CFD model responses (thick lines) with: (a) initial characteristic points and translation vectors, (b) comparison of the actual and the predicted (dash) high-fidelity response.

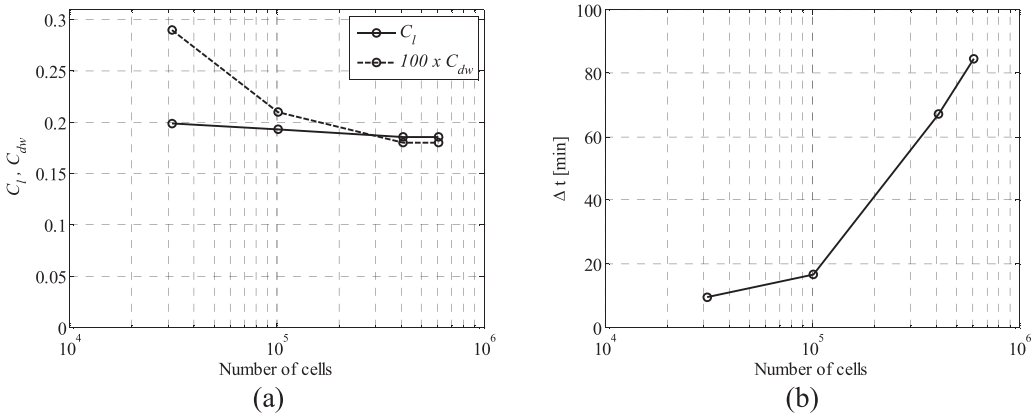

Fig. 8. Grid convergence study using the NACA 0012 airfoil (see Section 5.2) at Mach number $M_\infty = 0.75$ and angle of attack $\alpha = 1^\circ$; (a) lift and drag coefficients versus the number mesh cells and (b) the simulation time versus the number of mesh cells.

correcting the distributions obtained from the low-fidelity models to match the high-fidelity one, an alignment of the figures of interest of the models is uniquely obtained.

The main components of the SPRP surrogate are: the low-fidelity CFD model, the data obtained from a single high-fidelity CFD model evaluation, and a response prediction technique. Fig. 5 shows the overall process of the surrogate model construction using SPRP.

The pressure distribution for the high- and low-fidelity models will be denoted as $C_{p.f}$ and $C_{p.c}$, respectively. The surrogate model is constructed assuming that the change of $C_{p.f}$ due to the adjustment of the design variables x can be predicted using the actual changes of $C_{p.c}$. The change of $C_{p.c}$ is described by the translation vectors corresponding to a certain (finite) number of its characteristic points. These translation vectors are subsequently used to predict the change of $C_{p.f}$, whereas the actual $C_{p.f}$ at the current design, $C_{p.f}(x^{(i)})$, is treated as a reference. Fig. 6(a) shows the pressure distribution $C_{p.c}$ of the low-fidelity model for a NACA 2412 airfoil (see Section 5.2 for the details of this airfoil section) for $M_\infty = 0.7$ and $\alpha = 1^\circ$ (solid line), as well as $C_{p.c}$ at a different design, x (dashed line). $x^{(i)}$ will denote a current design (at the ith iteration of the optimization algorithm; the initial design will be denoted as $x^{(0)}$ accordingly). Circles denote characteristic points of $C_{p.c}(x^{(i)})$, here, representing, among others, x/c equal to 0 and 1 (leading and trailing airfoil edges, respectively), the maxima of $C_{p.c}$ for the lower and upper airfoil surfaces, as well as the local minimum of $C_{p.c}$ for the upper surface. The last two points are used for locating the pressure shock. Squares denote corresponding characteristic points for $C_{p.c}(x)$, while small line segments represent the translation vectors that determine the "shift" of the characteristic points of $C_{p.c}$ when changing the design variables from $x^{(i)}$ to x.

In order to obtain a reliable prediction, the number of characteristic points has to be larger than illustrated in Fig. 6(a). Additional points are inserted in between initial points either uniformly with respect to x/c (for those parts of the pressure distribution that are almost flat) or based on the relative pressure value with respect to corresponding initial points (for those parts of the pressure distribution that are "steep"). Fig. 6(b) shows the full set of characteristic points (initial points are distinguished using larger markers). The specific allocation of the additional characteristic points is not critical for the performance of the algorithm.

The pressure distribution of the high-fidelity model at a given design, here, x, can be predicted using the translation vectors applied to the corresponding characteristic points of the pressure distribution of the high-fidelity model at $x^{(i)}$, $C_{p.f}(x^{(i)})$. This is illustrated in Fig. 7(a), where only initial characteristic points and translation vectors are shown for clarity. Fig. 7(b) shows the predicted pressure distribution of the high-fidelity model at x as well as the actual $C_{p.f}(x)$. The agreement between both curves is very good. A rigorous formulation of the SPRP technique can be found in [8].

4. Computational fluid dynamics models

4.1. High-fidelity model

The flow is assumed to be steady and inviscid. The compressible Euler equations are taken to be the governing fluid flow equations.

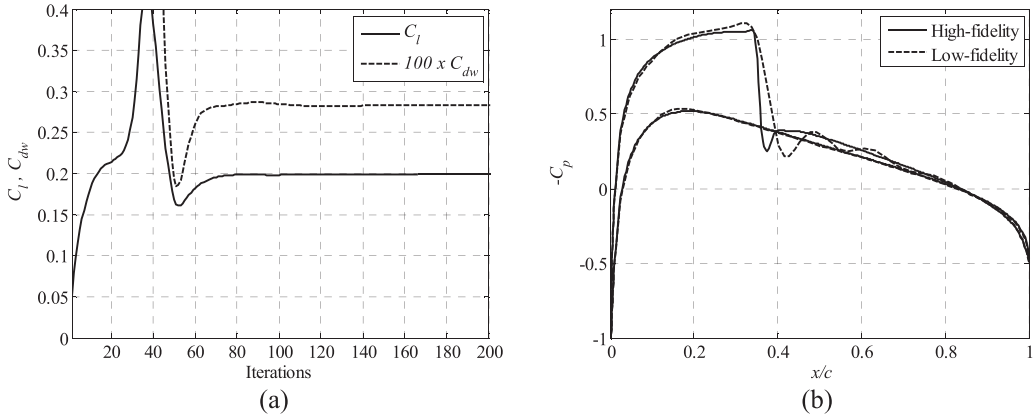

Fig. 9. Simulation results for the NACA 0012 airfoil (see Section 5.2) at Mach number $M_\infty = 0.75$ and angle of attack $\alpha = 1^\circ$; (a) evolution of the lift and drag coefficients obtained by the "coarser" low-fidelity model, (b) comparison of the pressure distributions obtained by the high- and low-fidelity models.

4.1.1. Grid generation

The computational meshes are of structured curvilinear body-fitted C-topology with elements clustering around the airfoil and growing in size with distance from the airfoil surface. The solution domain boundaries are placed at 25 chord lengths in front of the airfoil, 50 chord lengths behind it, and 25 chord lengths above and below it. The computer code ICEM CFD [35] is used for the mesh generation. The free-stream Mach number, static pressure, and angle of attack are prescribed at the farfield boundary.

4.1.2. Flow solver

The flow solver is of implicit density-based formulation and the inviscid fluxes are calculated by an upwind-biased second-order spatially accurate Roe flux scheme. Numerical fluid flow simulations are performed using the computer code FLUENT [36]. Asymptotic convergence to a steady state solution is obtained for each case. The iterative convergence of each solution is examined by monitoring the overall residual, which is the sum (over all the cells in the computational domain) of the L^2 norm of all the governing equations solved in each cell. The solution convergence criterion for the high-fidelity model is the one that occurs first of the following: a reduction in all the residuals by six orders of magnitude, or a maximum number of iterations of 1000.

4.1.3. Aerodynamic forces

The non-dimensional force coefficients parallel to the x- and z-axes, C_x and C_z, respectively, are calculated by integrating the pressure distribution C_p over the surface of the airfoil as

$$C_x = \oint C_p \sin\theta ds, C_z = \oint C_p \cos\theta ds \quad , (12)$$

where ds is the surface panel element of length and θ is the angle the panel makes relative to the x-axis. The lift coefficient C_l and the wave drag coefficient C_{dw} are calculated as

$$C_l = -C_x \sin\alpha + C_z \cos\alpha, C_{\mathrm{dw}} = -C_x \cos\alpha + C_z \sin\alpha. \quad (13)$$

4.1.4. Grid convergence

A grid convergence study was performed using the NACA 0012 airfoil (see Section 5.2 for the details of this airfoil section) at a Mach number $M_\infty = 0.75$ and an angle of attack $\alpha = 1^\circ$. The study, shown in Fig. 8, revealed that around 400,000 mesh cells are needed for mesh convergence. This mesh is taken to be the high-fidelity CFD model. The overall simulation time for the case considered is around 67 min on a quad-core Intel Xeon 2.67 GHz CPU with 18GB RAM (used in all computational experiments in this work). The flow solver reached a converged solution after 352 iterations. The other meshes required around 350–500 iterations to converge, except the coarsest mesh, which terminated after 1000 iterations, with the overall simulation time around 9.5 min.

4.2. Low-fidelity models

The low-fidelity CFD models are constructed in the same way as the high-fidelity model, but with a coarser computational mesh and relaxed convergence criteria. The two coarsest meshes shown in Fig. 8 are used as low-fidelity model meshes. The flow solution history for the coarser low-fidelity model, shown in Fig. 9(a), indicates that the lift and drag coefficients are nearly converged after 80–100 iterations. The maximum number of iterations is set to 100. This reduced the overall simulation time to 1.5 min. A comparison of the pressure distributions, shown in Fig. 9(b), indicates that the low-fidelity model, in spite of being based on much coarser mesh and reduced flow solver iterations, captures the main features of the high-fidelity model pressure distribution quite well. The biggest discrepancy in the distributions is around the shock on the upper surface, leading to an over estimation of both lift and drag (Fig. 8(a)). For the "finer" low-fidelity model, the number of iterations is set to 100 as well, and the evaluation time is around 3 min.

The mean ratio of simulation times of the high-fidelity model (f) to the coarsest low-fidelity model (c_1), with ~30,000 mesh cells, is $\mathrm{TR}_{c1} \approx 80$, and the corresponding value for the second coarsest low-fidelity model (c_2), with ~100,000 mesh cells, is $\mathrm{TR}_{c2} \approx 40$.

Table 1
Optimization results for Case 1.

Case 1 (lift maximization) $M_\infty = 0.75$, $\alpha = 0^\circ$, $C_{\mathrm{dw,max}} = 0.005$, $A_{\mathrm{min}} = 0.075$				
Variable	Initial	MLO	SM	SPRP
m	0.0200	0.0148	0.0150	0.0145
p	0.4000	0.7743	0.7463	0.7723
t/c	0.1200	0.1114	0.1140	0.1135
C_l	0.4745	0.5933	0.5650	0.5576
C_{dw}	0.0115	0.0050	0.0050	0.0050
A	0.0808	0.0750	0.0767	0.0767
N_c[a,b]	–	60/47	210	180
N_f[a]	–	2	4	6
Cost	–	~5	~7	~10

[a] N_c and N_f are the number of low- and high-fidelity model evaluations, respectively.
[b] ML uses coarse meshes c_1 and c_2 (given and N_{c1}/N_{c2} in the table). SM and SPRP both use c_1.

5. Numerical examples

5.1. Case descriptions

The three SBO algorithms described in Section 3 are applied to the same design cases. We consider three cases at transonic flow conditions. Case 1 involves lift maximization of an airfoil at a Mach number $M_\infty = 0.75$, and an angle of attack $\alpha = 0^\circ$. The maximum allowable drag coefficient is set $C_{\mathrm{dw.max}} = 0.005$, and the minimum non-dimensional cross sectional area is $A_{\mathrm{min}} = 0.075$. Case 2 involves drag minimization of an airfoil at $M_\infty = 0.70$ and $\alpha = 1^\circ$, with minimum lift coefficient $C_{l.\mathrm{min}} = 0.60$ and $A_{\mathrm{min}} = 0.075$. In Case 3, the lift coefficient is maximized at $M_\infty = 0.75$ and $\alpha = 1^\circ$ with $C_{dw.\mathrm{max}} = 0.0041$ and $A_{\mathrm{min}} = 0.065$.

The airfoil shapes are parameterized using the NACA (National Advisory Council of Aeronautics) four-digit airfoil with m (the maximum ordinate of the mean camber line as a fraction of chord), p (the chord-wise position of the maximum ordinate), and t/c (the thickness-to-chord ratio) as the design variables (full details of the NACA airfoil description can be found in Abbott and von Doenhof [37]). The bounds on the design variables are $0 \le m \le 0.1$, $0.2 \le p \le 0.8$, and $0.05 \le t/c \le 0.2$. Initial design for Cases 1 and 2, is NACA 2412 ($m = 0.02$, $p = 0.4$, $t/c = 0.12$), and for Case 3 is NACA 3210 ($m = 0.03$, $p = 0.2$, $t/c = 0.10$).

Optimization of the low-fidelity models is performed using the pattern-search technique in all algorithms.

5.2. Optimization results

Details of the test cases and optimization results are given in Tables 1–3. The header of the table gives the test case details, i.e., Mach number, angle of attack, and constraint values. The first 3 lines give the design variables (m, p, and t/c). Lines 4–6 give the performance characteristics (C_l, C_{dw}, and A). The last 3 lines give the optimization cost. The second column gives the values for the initial design and the next three columns give the results for each algorithm. Fig. 10 shows the pressure distributions of the initial and optimized shapes of Cases 1 and 2. Fig. 11 shows the Mach contour plots of the initial and optimized designs of Case 3.

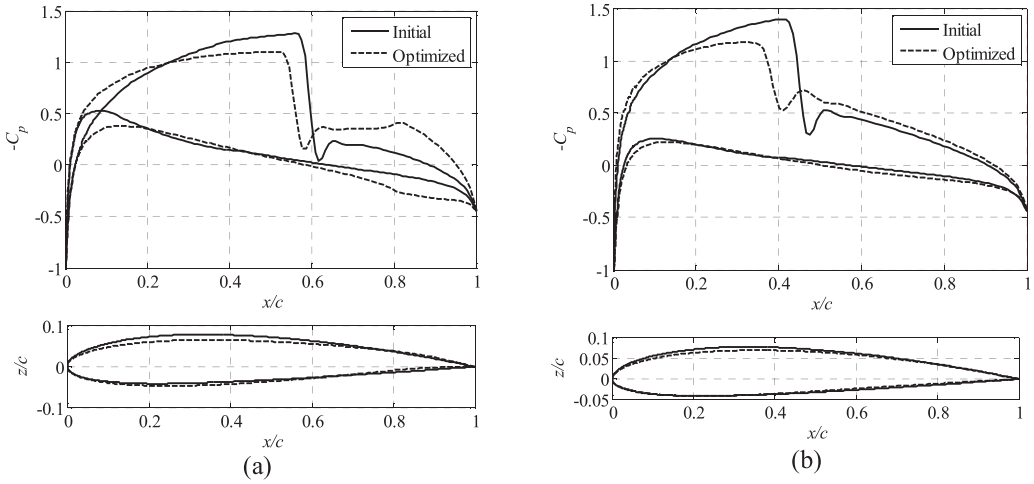

Fig. 10. Initial and optimized pressure distributions and airfoil shapes of: (a) Case 1 and (b) Case 2.

Table 2
Optimization results for Case 2.

Case 2 (Drag minimization)
$M_\infty = 0.70$, $\alpha = 1^\circ$, $C_{l,\min} = 0.60$, $A_{\min} = 0.075$

Variable	Initial	MLO	SM	SPRP
m	0.0200	0.0180	0.0180	0.0203
p	0.4000	0.6100	0.5290	0.4107
t/c	0.1200	0.1164	0.1113	0.1117
C_l	0.5963	0.6508	0.6002	0.6006
C_{dw}	0.0047	0.0024	0.0017	0.0032
A	0.0808	0.0784	0.0749	0.0753
N_c [a,b]	–	60/47	160	210
N_f [a]	–	2	3	7
Cost	–	∼5	5	∼12

[a] N_c and N_f are the number of low- and high-fidelity model evaluations, respectively.
[b] ML uses coarse meshes c_1 and c_2 (given and N_{c1}/N_{c2} in the table). SM and SPRP both use c_1.

Table 3
Optimization results for Case 3.

Case 3 (lift maximization)
$M_\infty = 0.75$, $\alpha = 1^\circ$, $C_{dw,\max} = 0.0041$, $A_{\min} = 0.065$

Variable	Initial	MLO	SM	SPRP
m	0.0300	0.0076	0.0100	0.0091
p	0.2000	0.6902	0.6929	0.7397
t/c	0.1000	0.1057	0.0980	0.0981
C_l	0.8035	0.4544	0.5281	0.5244
C_{dw}	0.0410	0.0041	0.0041	0.0041
A	0.0675	0.0712	0.0659	0.0660
N_c [a,b]	–	60/67	260	180
N_f [a]	–	2	5	7
Cost	–	∼6	∼9	∼11

[a] N_c and N_f are the number of low- and high-fidelity model evaluations, respectively.
[b] ML uses coarse meshes c_1 and c_2 (given and N_{c1}/N_{c2} in the table). SM and SPRP both use c_1.

The optimization cost is given in terms of the number model evaluations for the low- and the high-fidelity models, N_c and N_f, respectively, as well as the equivalent number of high-fidelity model evaluations is denoted by cost and is calculated as $N_f + N_c/\mathrm{TR}_c$, where TR_c is the simulation time ratio given in Section 4.2. These metrics provide a simple, general, and computational platform independent comparison of the relative efficiency of the algorithms.

In general, thinner airfoil sections lead to lower drag coefficients. The results reflect this fact as all the designs have the cross-sectional area constraint active. In all the cases, the optimized designs are obtained by reducing camber, placing the location of the maximum camber relatively aft, and reducing the thickness. As a result, the shock strength on the upper surface is reduced with a reduction in drag. At the same time, the pressure distribution opens up in the aft, leading to improved lift. These effects can be observed

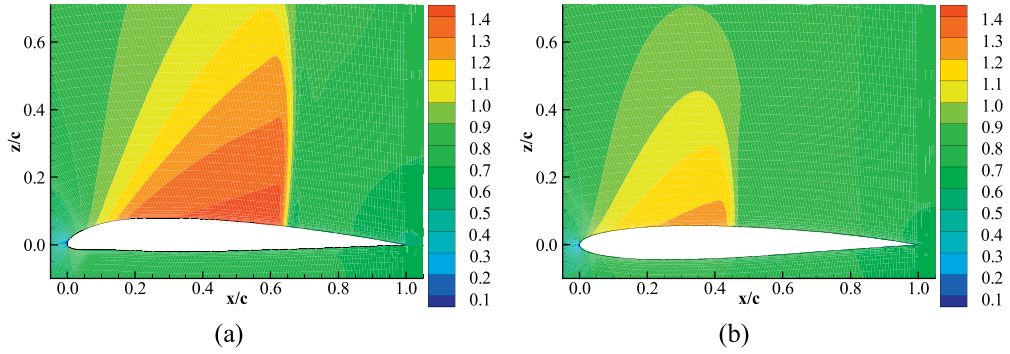

Fig. 11. Mach contour plots of Case 3 designs: (a) initial and (b) optimized.

in Fig. 10 for Cases 1 and 2. These geometry modifications are typical for the design of transonic airfoil sections and were expected. The reduction of the shock strength can also be observed in the Mach contour plot of Fig. 11, where the flow speed has been reduced dramatically from the initial to the optimized design.

In the three test cases, all the algorithms obtain similar designs in terms of the thickness-to-chord ratio (t/c), but the designs differ slightly in the maximum camber (m) and the location of maximum camber (p). As a result, the designs differ slightly in terms of their performance. The reason for this is the numerical noise implicit in the models.

There is, however, a significant difference in the computational cost of the algorithms. In all cases, the MLO algorithm is the fastest and requires less than 6 equivalent high-fidelity function evaluations. SM is the second fastest and requires less than 7 equivalent high-fidelity evaluations in Case 1, 5 in Case 2, and less than 9 in Case 3. SPRP is the slowest, requiring less than 10 evaluation in Case 1, less than 12 in Case 2, and less than 11 in Case 3.

Thus, for the particular selection of the test cases, the MLO algorithm is the most efficient one. The efficiency of MLO lies in its ability to quickly (i.e., at a low computational cost) approach the optimum airfoil geometry by exploiting information contained in the lower-fidelity models. While the other methods, SM and SPRP, also utilize low-fidelity models, the advantage of MLO seems to be the use of multiple models so that each iteration of the algorithm requires smaller number of model evaluations to converge.

On the other hand, it should be noted that SM is simpler to implement than MLO (only one low-fidelity model required). The SPRP algorithm, although not as good as neither MLO nor SM for transonic airfoil design, has an important advantage of working at the level of pressure distribution rather than directly aerodynamic forces. This makes SPRP an efficient method for inverse design where certain characteristics are defined a priori, for example the pressure distribution, which is a different approach for airfoil design than considered in this work (for further details see [38]).

6. Conclusion

A review of aerodynamic design using variable-fidelity optimization algorithms and computational fluid dynamic (CFD) models has been presented. We have discussed a multi-level design optimization algorithm, as well as space mapping and shape-reserving response prediction techniques. All three methods employ the same set of CFD models (from high- to low-fidelity), but differ in how the low-fidelity models are exploited and/or corrected. For algorithm performance illustration, two design cases of transonic airfoils were considered. The presented methods are demonstrated to yield optimized designs at a very low computational cost corresponding to a few evaluations of the high-fidelity CFD airfoil model. For the particular test set, the multi-level method turns out to be superior of the other two techniques in terms of computational cost.

References

[1] R.M. Hicks, E.M. Murman, G.N. Vanderplaats, An Assessment of Airfoil Design by Numerical Optimization, NASA TM X-3092, 1974.
[2] R.M. Hicks, P.A. Henne, Wing design by numerical optimization, J. Aircr. 15 (7) (1978) 407–412.
[3] S. Nadarajah, A. Jameson, A comparison of the continuous and discrete adjoint approach to automatic aerodynamic optimization, AIAA Paper 2000-0667 (2000).
[4] D.J. Mavriplis, Discrete adjoint-based approach for optimization problems on three-dimensional unstructured meshes, AIAA J. 45 (4) (2007).
[5] M. Nemec, D.W. Zingg, Newton–Krylov algorithm for aerodynamic design using the Navier–Stokes equations, AIAA J. 40 (2002) 1146–1154.
[6] H. Kim, S. Obayashi, K. Nakahashi, Aerodynamic optimization of supersonic transport wing using unstructured adjoint method, AIAA J. 39 (2001) 1011–1020.
[7] O. Pironneau, Optimal Shape Design for Elliptic Systems, Springer-Verlag, 1983, 2015.
[8] A. Jameson, Aerodynamic design via control theory, J. Sci. Comput. 3 (1988) 233–260.
[9] T.L. Holst, T.H. Pulliam, Transonic wing shape optimization using a genetic algorithm, Fluid Mech. Appl. 73 (2003) 245–252.
[10] B. Epstein, S. Peigin, Optimization of 3D wings based on Navier-Stokes solutions and genetic algorithms, Int. J. Comput. Fluid Dyn. 20 (2006) 75–92.
[11] M.D. Gunzburger, Inverse design and optimization methods, The Von Karman Institute for Fluid Dynamics Lecture Series (1997).
[12] J. Gatsis, D.W. Zingg, A fully-coupled Newton–Krylov algorithm for aerodynamic optimization, AIAA Paper 2003-3956 (2003).
[13] A. Iollo, G. Kuruvila, S. Ta'asan, Pseudo-time method for optimal shape design using the Euler equations, NASA CR 198,205 (1995).
[14] N.V. Queipo, R.T. Haftka, W. Shyy, T. Goel, R. Vaidyanathan, P.K. Tucker, Surrogate-based analysis and optimization, Prog. Aerosp. Sci. 41 (1) (2005) 1–28.
[15] A.I.J. Forrester, A.J. Keane, Recent advances in surrogate-based optimization, Prog. Aerosp. Sci. 45 (1–3) (2009) 50–79.
[16] T.W. Simpson, J. Peplinski, P.N. Koch, J.K. Allen, Metamodels for computer-based engineering design: survey and recommendations, Eng. Comput. 17 (2001) 129–150.
[17] S.R. Gunn, Support vector machines for classification and regression, in: Technical Report, School of Electronics and Computer Science, University of Southampton, 1998.
[18] A.I.J. Forrester, A. Sóbester, A.J. Keane, Multi-Fidelity Optimization via Surrogate Modeling, Proc. Royal Soc. A 463 (2007) 3251–3269.
[19] J.-C. Jouhoud, P. Sagaut, M. Montagnac, J. Laurenceau, A surrogate-model based multidisciplinary shape optimization method with applications to a 2D subsonic airfoil, Comput. Fluids 36 (2007) 520–529.
[20] C.J. Brooks, A.I. Forrester, A.I.J. Keane, S. Shahpar, Multi-Fidelity Design Optimization of a Transonic Compressor Rotor, 9th European Conf. on Turbomachinery Fluid Dynamics and Thermodynamics, Istanbul, Turkey, 2011.
[21] N.M. Alexandrov, R.M. Lewis, C.R. Gumbert, L.L. Green, P.A. Newman, Optimization with variable-fidelity models applied to wing design, in: 38th Aerospace Sciences Meeting & Exhibit, Reno, NV AIAA Paper 2000-0841, Jan, 2000.
[22] T.D. Robinson, M.S. Eldred, K.E. Willcox, R. Haimes, Surrogate-based optimization using multifidelity models with variable parameterization and corrected space mapping, AIAA J. Vol. 46 (2008).
[23] S. Koziel, L. Leifsson, Multi-level surrogate-based airfoil shape optimization, in: 51st AIAA Aerospace Sciences Meeting including the New Horizons Forum and Aerospace Exposition, Grapevine, Texas, January 7-10, 2013.
[24] S. Koziel, L. Leifsson, Knowledge-based airfoil shape optimization using space mapping, in: 30th AIAA Applied Aerodynamics Conference, New Orleans, Louisiana, June 25–28, 2012.
[25] S. Koziel, Leifsson, L, Transonic airfoil shape optimization using variable-resolution models and pressure distribution alignment, AIAA paper -3177, in: 29th AIAA Applied Aerodynamic Conference, Honolulu, Hawaii, June 27–30, 2011.
[26] S. Koziel, L. Leifsson, Surrogate-based aerodynamic shape optimization by variable-resolution models, AIAA J. 51 (1) (2013) 94–106.
[27] J.W. Bandler, Q.S. Cheng, S.A. Dakroury, A.S. Mohamed, M.H. Bakr, K. Madsen, J. Søndergaard, Space mapping: the state of the art IEEE Trans, Microwave Theory Tech. 52 (2004) 337–361.
[28] S. Koziel, L. Leifsson, Surrogate-based aerodynamic shape optimization by variable-resolution models, AIAA J. 51 (1) (2013) 94–106.
[29] S. Koziel, L. Leifsson, Adaptive response correction for surrogate-based airfoil shape optimization, in: 30th AIAA Applied Aerodynamics Conference, New Orleans, Louisiana, June 25–28, 2012.
[30] J.D. Anderson, Fundamentals of Aerodynamics, 5th Ed., McGraw-Hill Inc., New York, 2010.
[31] S. Koziel, J.W. Bandler, K. Madsen, A space mapping framework for engineering optimization: theory and implementation, IEEE Trans Microwave Theory Tech. 54 (Oct 10) (2006) 3721–3730.
[32] A.R. Conn, N.I.M. Gould, P.L. Toint, Trust Region Methods, MPS-SIAM Series on Optimization, 2000.
[33] N.M. Alexandrov, J.E. Dennis, R.M. Lewis, V. Torczon, A trust region framework for managing use of approximation models in optimization, Struct. Multi. Optim. 15 (1) (1998) 16–23.
[34] A.J. Booker, J.E. Dennis Jr., D.B. Frank, V. Torczon, M.W. Trosset, A rigorous framework for optimization of expensive functions by surrogates, Struct. Optim. 17 (Feb 1) (1999) 1–13.
[35] ICEM CFD ver. 14.0, ANSYS Inc. Southpointe, 275 Technology Drive, Canonsburg, PA 15317, 2012.
[36] FLUENT, ver. 14.0, ANSYS Inc. Southpointe, 275 Technology Drive, Canonsburg, PA 15317, 2012.
[37] I.H. Abbott, A.E. von Doenhoff, Theory of Wing Sections, Dover Publications, 1959.
[38] L. Leifsson, S. Koziel, S. Ogurtsov, Inverse design of transonic airfoils using variable-resolution modeling and pressure distribution alignment, Int. Conf. Comp. Sci. (2011), Singapore, June 1–3.

Leifur Leifsson received a Ph.D. degree in Aerospace Engineering from Virginia Tech, USA, in 2006. He is currently an Associate Professor with the School of Science and Engineering at Reykjavik University (RU), Iceland. Leifur is the director of the Laboratory for Unmanned Vehicles at RU. His research interests include applied aerodynamics, surrogate-based modeling and optimization, multidisciplinary design optimization, and unmanned vehicle design. Prior coming to RU, Leifur held positions at Airbus UK Ltd., and Hafmynd Ltd.

Slawomir Koziel received the M.Sc. and Ph.D. degrees in electronic engineering from Gdansk University of Technology, Poland, in 1995 and 2000, respectively. He also received the M.Sc. degrees in theoretical physics and in mathematics, in 2000 and 2002, respectively, as well as the Ph.D in mathematics in 2003, from the University of Gdansk, Poland. He is currently a Professor with the School of Science and Engineering, Reykjavik University (RU), Iceland. He is the director of the Engineering Optimization & Modeling Center, RU. His research interests include CAD of microwave circuits, surrogate-based modeling and optimization, circuit theory, and numerical analysis.